# Unprecedented high photocatalytic activity of nanocrystalline WO₃/NiWO₄ hetero-junction towards dye degradation: Effect of template and synthesis conditions

Mohamed Mokhtar Mohamed [b,*], Saleh A. Ahmed [a], Khalid S. Khairou [a]

[a] Umm Al Qura University, Faculty of Applied Science, Chemistry Department, Makkah, Saudi Arabia
[b] Benha University, Faculty of Science, Chemistry Department, Benha, Egypt

ABSTRACT

Nanocrystalline NiWO₄ wolframite structure has been prepared by a simple salt solution addition (NiW₁SS), co-precipitation (NiW₄Cop) and sol–gel (NiW₄SG) techniques via employing polymeric templates particularly polyethylene glycol (PEG) and triblock copolymer, respectively. The synthesis method as well as the metal molar ratio (W/Ni) influenced the phases, morphology, optical and surface properties of synthesized samples as configured by X-ray diffraction, transmission electron microscopy, UV–vis diffuse reflectance spectroscopy, infrared spectroscopy, X-ray photoelectron spectroscopy and N2 sorptiometry techniques. Accordingly, the NiW₁SS material that exposed only NiWO₄ of nano-plate shape at a molar ratio (W/Ni) 1 indicates higher surface texturing values ($S_{BET} = 52.6 \, m^2/g$, $V_p = 0.2061 \, cm^3/g$ and $r = 15.7 \, nm$) exceeding those of NiW₄Cop ($S_{BET} = 15.07 \, m^2/g$, $V_p = 0.0491 \, cm^3/g$ and $r = 13.0 \, nm$) of anisotropic shapes (hexagonal and tetragonal); synthesized at a ratio of 4 and by the same template (PEG). The NiW₁SS material indicated $E_g$ value of 2.23 eV whereas that of NiW₄Cop revealed a value of 2.92 eV. On the other hand, NiW₄SG that exposed well crystallized WO₃ beside NiWO₄ of nano-flakes shape and an average diameter of 25 nm indicates $E_g$ value of 2.56 eV and in addition evokes the formation of narrow pore size distribution in mesopores range (2–12 nm) as well as in macropores (60 nm) exploring the effect of template type on the pore texturing. Photodegradation of methylene blue (MB) dye was used to evaluate the photoactivity of NiWO₄ catalysts under UV irradiations. The NiW₄SG catalyst exhibited the best degradation performance (92.5% for MB after 5 h). The results showed that the feasibility of MB degradation was not only due to morphological properties but also to the NiWO₄/WO₃ heterojunction. Significantly, WO₃ facilitates effective charge separation as traced by the photoluminescence emission spectra.

© 2013 Elsevier B.V. All rights reserved.

## 1. Introduction

Transition metal tungstates have many applications, such as in gas sensors, optical fibres, humidity sensors, pigments and catalytic reactions [1–5]. Among these tungstates, nickel tungstate (NiWO₄) has been extensively studied. Mixed nickel–tungsten oxide, denoted as NiWO₄, may have properties that are superior to those of the two components. NiWO₄ has important electrochromic properties, besides a high long-lasting structural stability [6] and good catalytic properties [7]. The later tungstate crystallizes with wolframite structure that has monoclinic unit cell and space group P2/c characterized by alternating layers of nickel and tungsten atoms parallel to the (1 0 0) plane [8]. The coordination around

tungsten and nickel atoms is six, giving ribbons of like-filled octahedra sharing edges but unlike octahedra share corners [9]. In this way W₂O₈ structural units are formed in NiWO₄ similar to those of the CdWO₄ compound [10]. Usually single crystalline NiWO₄ can be prepared by solid state synthesis at high temperature [11,12] by co-precipitation from aqueous solutions of soluble salts [13,7] and by microwave assisted synthesis [14]. Several methods of chemical synthesis, on the other hand, have gained popularity for preparation of ceramic oxides including tungstates such as sol–gel, hydrothermal, citrate gel, polymeric precursors and gel combustion [15,16]. Chemical and physical properties of metal oxides and in particular tungstates are generally dependent on the synthesis route. Although transition metal tungstates have sufficient chemical and thermal stability [17,18] very few reports are available in the literature regarding their uses as photocatalysts for environmental remediation. Recently, the appreciable activity of ZnWO₄ for the degradation of Rhodamine B was

* Corresponding author.
  E-mail address: mohmok2000@yahoo.com (M.M. Mohamed).

reported [19–21]. Enhancement of the photocatalytic activity of $ZnWO_4$ doped with fluoride ions was also observed but never exceeds 10% [22]. Accordingly, the main objective is to elucidate the structural evolution of the phases that emerge when an atomic ratio of W/Ni equals 4 via employing polymeric precursors including triblock copolymer and polyethylene glycol. This is intentionally performed to see to what extent the presence of $WO_3$ will affect the structure, morphology as well as the photocatalytic performances of $NiWO_4$. Sol–gel, co-precipitation and facile salt solution addition techniques were successfully used in the synthesis of nickel tungstate nanoparticles of controlled morphologies. Hence, the present work is aimed at studying the phases, morphology, optical, surface properties and structural transformations of the produced $NiWO_4$ compound using X-ray diffractometry (XRD), TEM, X-ray photoelectron spectroscopy (XPS), UV–vis diffuse reflectance spectroscopy, photoluminescence, and FTIR spectroscopy beside surface texturing properties ($N_2$ adsorption). In addition, the photoactivity of as-synthesized nanoparticles will be tested for the degradation of methylene blue (MB) dye.

## 2. Experimental

### 2.1. Catalysts preparation

#### 2.1.1. Preparation of $NiWO_4$ by an atomic ratio (W/Ni) of 1 using simple addition method

Analytical-grade nickel nitrate and sodium tungstate were used as received from Merck Company. The $NiWO_4$ was formed by precipitating a stoichiometric mixture of sodium tungstate and nickel nitrate solutions according to the following procedure. $Na_2WO_4 \cdot 2H_2O$ (32.9 g) dissolved in 100 ml of distilled water containing polyethylene glycol-2000 [$(HO(CH_2CH_2O)_nH)$-PEG 2000-2 g/100 ml water)] was poured on $Ni(NO_3)_2 \cdot 6H_2O$ dissolved in PEG (29.0 g/100 ml water PEG). Following addition, a green precipitation was formed while vigorous stirring. The precipitate was left for one day, filtered, and washed with distilled water for several times. Then, dried at 110 °C for 5 h and finally calcined at 400 °C for 6 h to obtain $NiWO_4$. This sample was denoted as $NiW_{1SS}$ where 1 corresponds to a W/Ni atomic ratio of 1 where SS represents salt solution by which the catalyst was simply synthesized.

#### 2.1.2. Preparation of $NiWO_4$ by an atomic ratio (W/Ni) of 4 using co-precipitation method

Ni was first dissolved in water containing PEG-2000 (100 ml) and same for $Na_2WO_4$. The later solution was poured onto the former under vigorous stirring to produce a blue suspension. Ammonia solution (15%) was then added into the suspension in a drop wise manner until complete precipitation followed by heating at 85 °C for 6 h. The blue suspension was changed into green precipitate which filtered, washed with excess water and dried at 110 °C for 10 h. Calcinations at 400 °C for 6 h were accomplished. This sample was denoted as $NiW_{4Cop}$, where 4 accounts for the atomic ratio of 4/1 (W/Ni) and Cop accounts for the used method co-precipitation.

#### 2.1.3. Preparation of $NiWO_4$ by an atomic ratio (W/Ni) of 4 using sol–gel method

Appropriate amounts of $Na_2WO_3$ and $Ni(NO_3)_2$ were used so as to obtain a 4:1 atomic ratio in the final product. Sodium tungstate was first dissolved in triblock copolymer-pluronic 123 [consisting of (ethylene oxide)$_{20}$ (propylene oxide)$_{70}$ (ethylene oxide)$_{20}$] – solution (1 g/100 ml)] followed by pH adjustment to a value of 8.8 via drop-wise addition of ammonia solution (15%, v/v). On the other hand, the solution of nickel nitrate dissolved also in

the triblock copolymer (1 g/100 ml) was added to that of the latter and thus the reacting solutions were kept at 60 °C under vigorous stirring until a gel was formed. After gelation for 24 h in Teflon lined autoclave at the same temperature (60 °C), the gel was dried at 110 °C over night then calcined at 400 °C for 6 h. This sample was denoted as $NiW_{4SG}$ where SG is accounted for the sol–gel method of preparation.

### 2.2. Catalyst characterization

#### 2.2.1. X-ray diffraction analysis

X-ray diffraction analysis was performed on X-ray diffractometer (XRD) Model XRD 8030 from Jeol Co., Japan. Maximum power is 3 kW and the unit is equipped with rotating stage and thin layer accessories. The patterns were run with co-filtered CoKα radiation ($\lambda$ = 1.79 Å) energized at 45 kV, and 10 mA. The samples were measured at room temperature in the range of $2\theta$ = 10–80°. The XRD phases present in the samples were identified with the help of ASTM Powder Data Files.

#### 2.2.2. Transmission electron microscopy (TEM)

The nanostructured morphologies of the samples were examined using high resolution transmission electron microscopy (HRTEM) obtained by Tecnai G2 supper twin USA, with an accelerating voltage of 200 kV. The elemental composition of the composite material was investigated by energy-dispersive X-ray attached to the TEM equipment. The average particle diameter ($d$) was calculated by the following formula: $d = \Sigma n_i d_i / \Sigma n_i$, where $n_i$ is the number of particle diameter $d_i$ in a certain range, and $\Sigma n_i$ is more than 200 $NiWO_4$ particles on TEM images of the sample. Computer-assisted counting of nanoparticle images and automated image analysis based software package including KONTRON KS 400 (Zeiss-Kontron) was used. To show how much variation from the average the calculated standard deviation of all nanoparticle sizes is stated in the text of this paper.

#### 2.2.3. Fourier transform infrared spectra (FT-IR)

The infrared spectra of the samples were recorded in the range of 400–1000 cm$^{-1}$. The method includes mixing few milligram of a fine powder of the sample with KBr powder in an agate mortar. The mixture was then pressed by means of hydraulic press. The transmission was automatically registered against wavenumber (cm$^{-1}$) using a Perkin-Elmer instrument (Spectrum GX), made in USA.

#### 2.2.4. Nitrogen adsorption measurements

Nitrogen adsorption measurements were performed at liquid nitrogen temperature with a Micromeritics ASAP 2020 surface area and porosity analyzer. Prior to the measurements, the samples were degassed for half an hour at 363 K followed by 3 h at 473 K. Surface area was calculated using the BET (Brunauer–Emmett–Teller) interpretation of the nitrogen adsorption isotherm.

#### 2.2.5. UV–vis diffuse reflectance spectroscopy

Diffuse reflectance UV–vis spectroscopy (UV–vis DRS) of powder samples was carried out at room temperature using a PerkinElmer Lamda-900 spectrophotometer in the range of 200–800 nm. The UV–vis spectra were processed with Microsoft Excel software, consisting of calculation of the Kubelka–Munk function, $F(R_\infty)$, which was extracted from the UV–vis DRS absorbance. The edge energy ($E_g$) for allowed transitions was determined by finding the intercept of the straight line in the low-energy rise of the plot of $[F(R_\infty)hV]^2$, for the direct allowed transition, vs. $hV$, where $hV$ is the incident photon energy.

### 2.2.6. Photoluminescence spectroscopy

The PL spectra were recorded by photoluminescence (PL) spectrometer (Spectro Fluorescence JASCO fp-6200) using 290 nm as excitation wavelength at room temperature via pulsed YAG:Nd laser excitation.

### 2.2.7. X-ray photoelectron spectroscopy (XPS)

X-ray photoelectron spectroscopy (XPS) measurements were taken on the Thermo Scientific Escalab 250Xi spectrometer equipped with an MCD-9 detector and XR6 monochromatic source. This offers a user-selectable spot size from 200 to 900 μm. Automated in-lens irises may also be used to reduce the analysis area, offering a range of 300–20 μm. Spectra treatment were performed using the CASA software. The dual ion/electron flood source charge neutralization system, using very low energy electrons and ions, was used for the analysis of insulating samples. Typically the hydrocarbon C 1s line at 284.8 eV was used for energy referencing. All data processing (quantification, peak fitting, image generation, PCA, average spectrum generation, etc.) was performed within the Avantage data-system.

### 2.3. Photocatalytic activity

The photocatalytic properties of the various samples were evaluated by monitoring the degradation of methylene blue (MB, 350 ml, 20 ppm) dye in the presence of 200 mg of catalyst at room temperature. $TiO_2$ (P25, 20% rutile and 80% anatase) purchased from ACROS was tested as well for comparison purposes. All photodegradation experiments were performed in two side arms quartz photochemical reactor fitted with a cooling jacket. 125 W UV high pressure mercury lamp transmitted light in the wavelength range of 295–390 nm fitted with long Teflon tube was inserted into the reaction solution. Prior to irradiation, the catalyst and methylene blue solution were allowed to stir in the dark for 30 min prior to illumination to allow for adsorption of the methylene blue onto the surface of the catalyst. Aliquots of the solution were collected at different time intervals for a total of 400 min. The centrifuged aliquots were directed to UV–vis spectrophotometer to check the degradation of methylene blue dye via its absorption peak at 665 nm. This absorption data was used in the determination of degradation of the dye through comparison with the absorbance at a certain time as a percentage of the initial absorbance.

## 3. Results and discussion

### 3.1. XRD and TEM investigations

The XRD patterns of calcined samples are shown in Fig. 1. The pattern of $NiW_{4Cop}$ indicates the main diffraction peaks of monoclinic $NiWO_4$ phase at $2\theta = 65.9°, 54.7°, 52.4°, 49°, 41.8°, 36.6°, 31.0°, 25.0°,$ and $24.0°$ [JCPDS: 15-0755] which correspond to the (3 1 1), (2 0 2), (1 3 0), (0 0 2), (1 0 2), (2 0 0), (1 1 1), (1 1 0) and (0 1 1) crystallographic planes, respectively. Very small lines at $2\theta = 16°, 17°, 28°$ and $33.2°$ have also been included and ascribed to $WO_3$ of low crystallinity [23]. The XRD pattern of $NiW_{1SS}$ reveals diffraction peaks typical to those of $NiWO_4$ seen in $NiW_{4Cop}$. Diffractions of the later indicate much lower crystallinity than that of the former suggesting a decrease in crystallites size of $NiWO_4$ in $NiW_{4Cop}$ comparatively. In conformity, the particles size assessed using Scherrer equation based on using the (1 1 1) reflection at $31.0°$ were found to be 42 and 48 nm for $NiW_{4Cop}$ and $NiW_{1SS}$, respectively (Table 1). This indeed indicates that the $NiWO_4$ formed by the simple method at an atomic ratio of (W/Ni) 1 initiates nearly pure monoclinic $NiWO_4$ phase with negligible amount of low crystalline $WO_3$ phase [23] unlike the case in $NiW_{4Cop}$. The $NiW_{4SG}$ sample shows typical diffraction peaks of monoclinic $NiWO_4$ phase of lower intensities than that
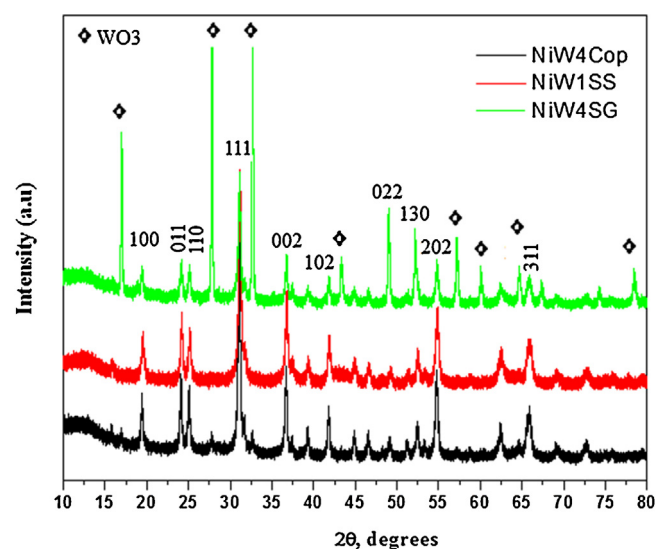


**Fig. 1.** XRD patterns of $NiW_{1SS}$, $NiW_{4SG}$ and $NiW_{4Cop}$.

in $NiW_{1SS}$, and thus indicates particles size comprised of 35 nm. Very strong peaks at $2\theta = 28.2°, 32.8°, 43.5° 57°, 60°, 64.8°$ and $78.7°$ were also depicted in this sample, characterizing highly crystalline $WO_3$ phase (JCPDS card 43-1035). This reflects the role played by the polymer template in growing one phase while retarding the other. An exhibited strong interaction between W ions and PEG in $NiW_{4Cop}$ is attained; and hence low crystalline $WO_3$ is emerged together with the highly crystallized $NiWO_4$ phase. On the contrary, promotion of $NiWO_4$ formation in $NiW_{4SG}$ with low crystallinity together with well crystallized $WO_3$ phase admits that a quite weak interaction between W ions and the triblock copolymer template is proposed. Accordingly, the tendency of the template to interact with the excess of W ions in the nominal molar ratio of 4 (W/Ni) affects the phases produced ($NiWO_4$ and $WO_3$) as well as their percentages in $NiW_{4Cop}$ and $NiW_{4SG}$.

The morphologies of $NiWO_4$ samples were examined by TEM. The TEM image of $NiW_{1SS}$ shown in Fig. 2a revealed a nanoplates-like structure with an average size of $40 \pm 3$ nm. The inset in the figure illustrates the SAED pattern of $NiWO_4$ nanocrystals that perfectly indexed to a monoclinic wolframite structure, via the existed facets at (1 1 1), (2 0 0) and (3 1 1) [24]. This was in good agreement with the XRD results. The pattern of $NiW_{1SS}$ shows rings, characteristic of nanocrystalline materials, with some scattered ones. The EDS spectrum, with elemental analysis, of this sample indicates (not shown) 50% of C, 33.6% of O, 8.3% of Ni and 8.1% of W on the surface. The ratio of W/Ni is stoichiometrically equal 1 as planned during the synthesis process.

The TEM image of $NiWO_{4Cop}$ exhibits anisotropic shapes of hexagonal and tetragonal nanoplates with an average diameter of $34 \pm 2$ nm and length of 25–55 nm. The corresponding SAED pattern of the sample, shown as inset in Fig. 2b, indicates diffraction rings ascribed to (1 1 1), (2 0 0) and (3 1 1) of $NiWO_4$ crystalline phase. The corresponding EDS spectrum of the sample indicates (not shown) 36.5% of C, 20.1% of O, 4.6% of Ni, 19.9% of Cu and 18.8% of W. The content of Ni and W was near to the nominal value of 1:4 as intentionally suggested during the preparation. The presence of Cu was due to the copper grid used in the TEM measurements. Although the percentages of C is lower than that in $NiW_{1SS}$ we cannot neglect the carbon impurities derived from the non-complete decomposition of the PEG template that has been ascertained using the TG technique (not shown).

**Table 1**
Surface texturing, particles size and phases of synthesized $NiWO_4$ catalysts.

| Sample name | $S_{BET}$ $(m^2/g)$[a] | $V_p$ $(cm^3/g)$[b] | $r$ $(nm)$[c] | Particle size $(nm)$[d] | Composed phases[e] |
|---|---|---|---|---|---|
| $NiW_{1SS}$ | 52.6 | 0.2061 | 15.7 | 48 | $mNiWO_4 + nLcWO_3$ |
| $NiW_{4Cop}$ | 15.1 | 0.0491 | 13.2 | 42 | $mNiWO_4 + LcWO_3$ |
| $NiW_{4SG}$ | 4.7 | 0.0164 | 13.9 | 35 | $mNiWO_4 + HcWO_3$ |

[a] $S_{BET}$, BET surface area.
[b] $V_p$, pore volume.
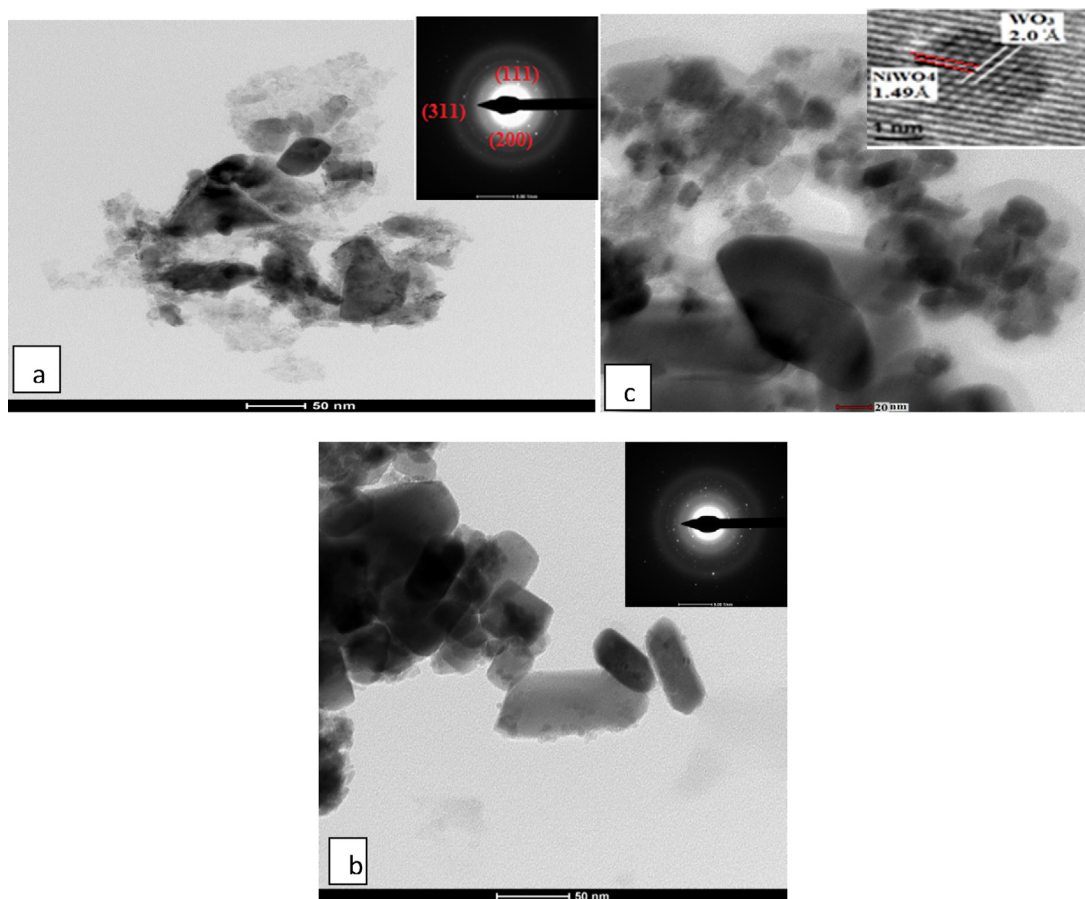[c] $r$, BJH adsorption average pore diameter.
[d] Crystallite sizes determined by the broadening of the $NiWO_4$ (1 1 1) facet diffraction peak using the Scherrer formula.
[e] Composed phases where m denoted for monoclinic, nLc for negligible amount of low crystalline, Hc for high crystalline and Lc for low crystalline.

The TEM image of $NiW_{4SG}$ shows irregular crystalline nano-flakes structure with average sizes of $25 \pm 2$ nm. The HRTEM-inset in this figure shows distances at 2.0 Å and 1.49 Å, which correspond to (2 2 2) and (1 1 1) planes of $WO_3$ and $NiWO_4$ phases, respectively. This signifies the close proximity of the two phases. This close interconnection between the two phases is supposed to favour the photoinduced electrons transfer between the phases that assume to reduce the recombination of the photoinduced electrons and holes, and improve the photocatalytic activity of the catalysts. The corresponding EDS pattern of the sample indicates that the elemental composition of W/Ni ratio was lower than 4 proposing that W was not exposed on the surface. Decreasing the particle size of this sample comparatively explains the role of triblock copolymer template in slowing the nucleation rate via the sol–gel technique however resulted in non-homogeneous nucleation so as to producing such irregular flaky structure.

## 3.2. Surface texturing properties

Fig. 3 shows the $N_2$ adsorption–desorption isotherms of the mixed oxide composites calcined at 400 °C. They belong to type II according to the IUPAC classification. The non-limiting adsorption at high $P/P^0$ is characteristic of Type H3 loop. The BET analysis revealed that the $NiW_{1SS}$ sample exhibits higher surface area of 52.6 $m^2/g$ exceeding 15.07 $m^2/g$ of $NiW_{4Cop}$ and 4.7 $m^2/g$ of $NiW_{4SG}$ (Table 1). It has been reported that both pure NiO and $WO_3$ exhibit low surface area (4 and 9 $m^2/g$, respectively) values [25,26]. Accordingly, the enhancement in surface area particularly in $NiW_{1SS}$ is likely due to the presence of the PEG template that hinder the crystallization of NiO and $WO_3$ preventing the formation of large particles. The pore-size distribution obtained for $NiW_{1SS}$ acquired from $N_2$ adsorption indicates that it's composed of mesoporous distribution centred at 250 Å. The pore size distribution obtained for



**Fig. 2.** TEM image of (a) $NiW_{1SS}$; (b) TEM image of $NiW_{4Cop}$, the inset in (a) and (b) shows the corresponding SAED patterns; (c) TEM image of $NiW_{4SG}$ with HRTEM inset figure.
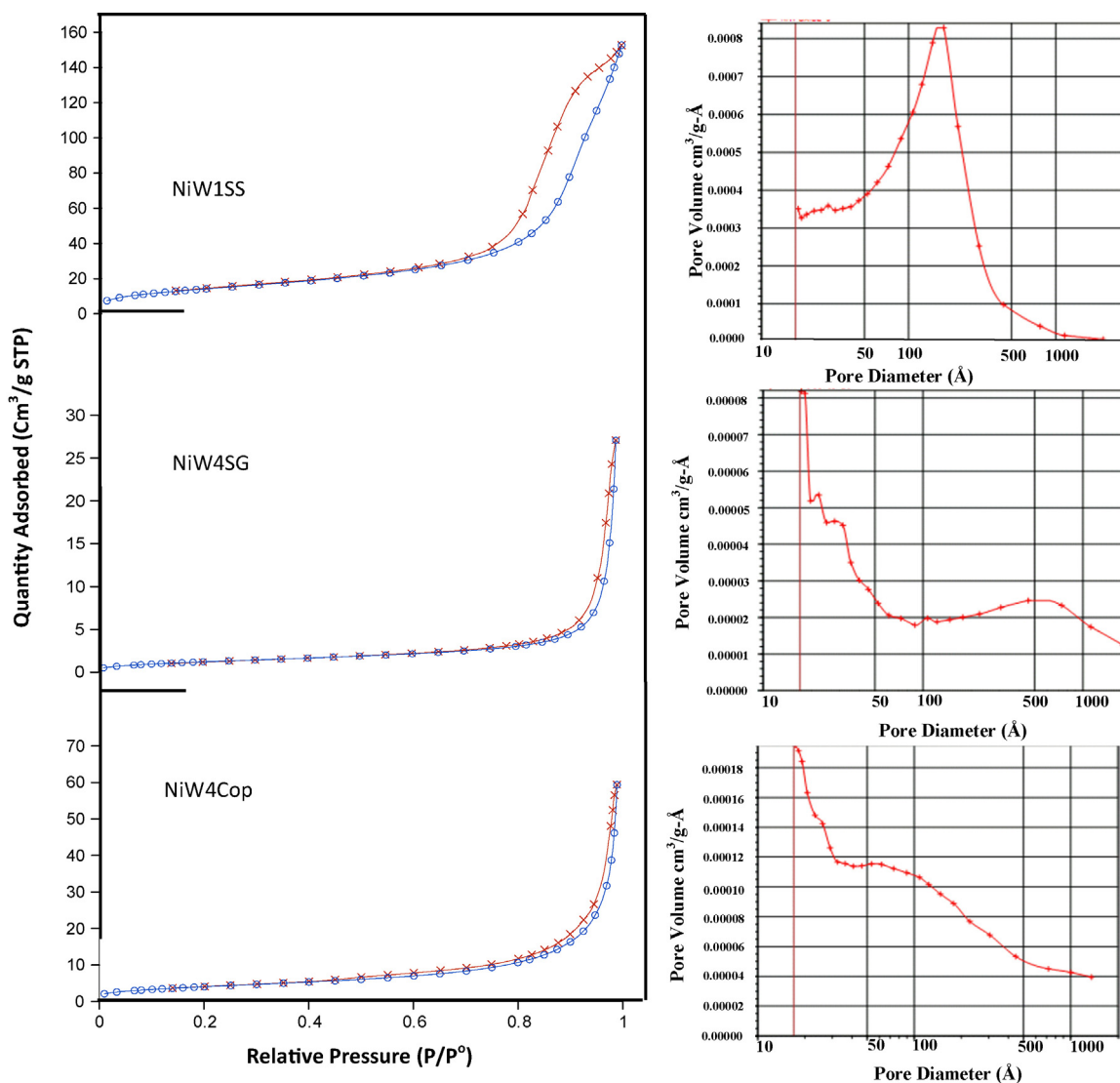
**Fig. 3.** Adsorption–desorption isotherms and pore size distribution of $NiW_{1SS}$, $NiW_{4SG}$ and $NiW_{4Cop}$.

$NiW_{4SG}$ indicates that it's composed of mesopores with quite narrow distributions centred at 20, 30 and 120 Å, as well as macropores centred at 600 Å, seen as a broad band. Such macropores explain the reason for the marked decrease in $S_{BET}$ of this particular sample. In addition, deposition of residual amounts of non-decomposed triblock copolymer moieties in the pores of $NiW_{4SG}$ affects the pore volume [0.0164 cm³/g for $NiW_{4SG}$ vs. 0.0491 cm³/g for $NiW_{4Cop}$ and 0.2061 cm³/g for $NiW_{1SS}$ (Table 1)] that by in turn affects the surface area value. On the contrary, $NiW_{4Cop}$ showed a bimodal distribution centred at 25 Å; as a shoulder, together with a broad one centred at 60 Å. The shape of the nitrogen adsorption–desorption isotherm is strongly influenced by the W/Ni atomic ratio, e.g. in the 1:1 ratio; as in $NiW_{1SS}$, mesopores were only existed with larger hysteresis loop than $NiW_{4Cop}$ synthesized using the same template (PEG) but with varied atomic ratio (W/Ni = 4). This let us presume that in the $NiW_{1SS}$ sample, PEG 2000 has been well assembled in a facile way to form large ordered mesoporous $NiWO_4$ whereas this ordering is somehow narrowed when the atomic ratio raised to 4 in $NiW_{4Cop}$. This probably due to the absence of $WO_3$ moieties in the $NiW_{1SS}$ sample as depicted from XRD results unlike the case in the other samples. $NiW_{4SG}$ revealed a combination of both meso- and macropores whereas $NiW_{4Cop}$ displayed only a lower margin of mesopores. $NiW_{4SG}$ and $NiW_{4Cop}$ samples presented

similar adsorption–desorption isotherm except that the desorption step in the former was at $P/P^0 = 0.85$ where it was at 0.55 for the later reflecting that varying the polymeric template from triblock to polyethylene glycol affects the ink-bottle type of pores ($P/P^0 > 0.5$) [27,28] produced for the shaped $NiWO_4$. Narrowing parts of the mesoporous channels and creating ink-bottle like sections can be recognized in the $NiW_{4SG}$ sample and as a result a trimodal distribution is revealed at 20, 30 and 120 Å upon employing the triblock copolymer template. Deposition of $WO_3$ and/or carbons in the pore structure of the formed $NiWO_4$ phase can produce such small distributions, as has been affirmed from HRTEM results of this sample that showed the close contact between both phases ($WO_3$/$NiWO_4$).

### 3.3. Optical and vibrational properties

The optical properties of the samples are characterized by UV–vis spectroscopy (Fig. 4). Four absorption bands at 329, 382, $455_{sh}$ and 739 nm are observed in $NiW_{1SS}$. It has been reported that crystalline $NiWO_4$ exhibits an adsorption band at 450 nm as well as at 342 nm [28] whereas $WO_3$ displays an absorption band at 718 nm [29]. Accordingly, by matching, the absorption band positioned at 382 nm constitutes with those depicted at 329 and $455_{sh}$ nm the formation of $NiWO_4$ since neither $WO_3$ nor NiO has
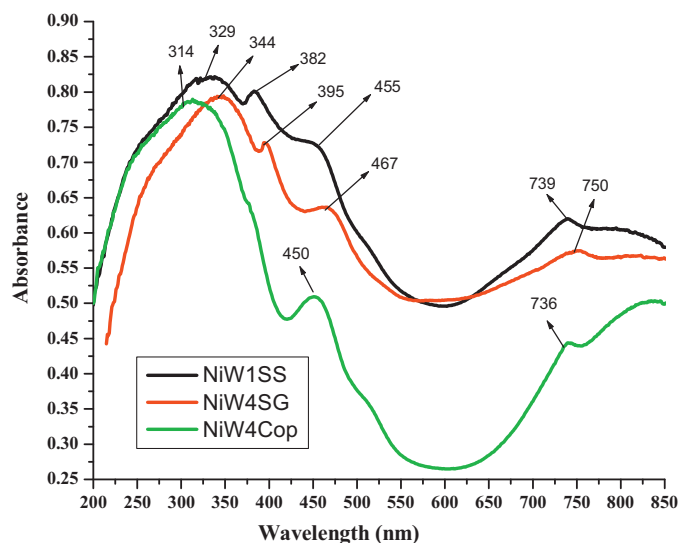
**Fig. 4.** UV–vis DRS spectra of NiW$_{1SS}$, NiW$_{4SG}$ and NiW$_{4Cop}$.

absorption bands around the wavelength at 382 nm. Assigning the band at 739 nm into WO$_3$ matching that at 718 nm [30] was not in agreement with XRD data indicating that the formed WO$_3$ phase in NiW$_{1SS}$ was in amorphous state, rather than in crystalline one. Similarly, the NiW$_{4Cop}$ sample indicates similar bands as shown for NiW$_{1SS}$ but at lower wavelengths (314, 450 and 736 nm) together with vanishing that at 382 nm. The NiW$_{4SG}$ sample indicates the same bands as in NiW$_{1SS}$ except that significant enhancement to visible light bands was revealed. The bands at 329, 382 and 455 nm ascribed to NiWO$_4$ in NiW$_{1SS}$ are shifted into 344, 395 and 467 nm, respectively in NiW$_{4SG}$. This shift to higher wavelengths is probably related to the dispersed particles and to the difference in particles size of NiW$_{4SG}$ compared to NiW$_{1SS}$, [31] as illustrated in XRD and TEM investigations. Meanwhile, UV–vis results revealed that NiWO$_4$ nano-particles have good light absorption properties not only in the UV region but also in the visible light ones. Shifting the WO$_3$ band at 739 nm in NiW$_{1SS}$ into 750 nm in NiW$_{4SG}$ was in conformity with the conclusion obtained from XRD data stating that NiW$_{4SG}$ owns the highest crystallized WO$_3$ phase between all samples. This declares that UV–vis spectroscopy is rather sensitive in detecting the existence of any crystalline WO$_3$ phase.
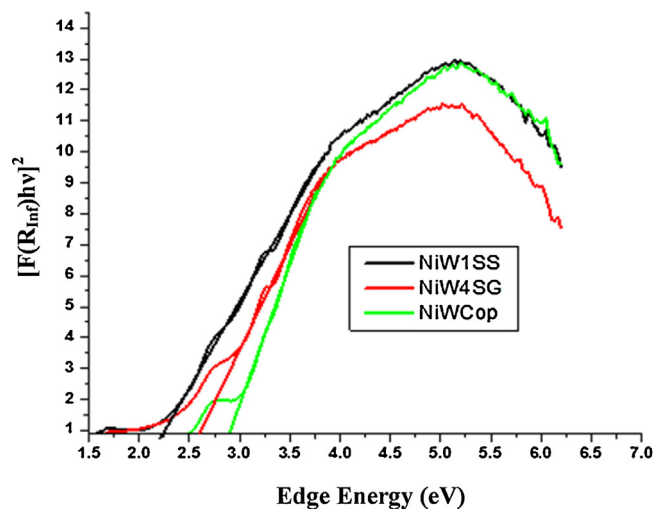
In order to determine $E_g$, we have analyzed the measured absorption spectra of the studied tungstates, by calculating the absorption edge as depicted in Fig. 5. The values of optical transition obtained by extrapolating the straight line portion to energy axis at zero absorption coefficients give the direct optical band gaps. In particular, we found that $E_g$ decreases in the following sequence NiW$_{4Cop}$ > NiW$_{4SG}$ > NiW$_{1SS}$. For NiW$_{4SG}$, the determined $E_g$ (2.53 eV) agreed well with the value reported in the literature [32]. In case of NiW$_{1SS}$, the measured $E_g$ is 2.23 eV. This suggested that the band-gap energy of NiWO$_4$ synthesized by the simple addition via employing PEG-2000 was much lower than the previously accepted value (2.56 eV) [33] whereas that calculated for NiW$_{4Cop}$ was 2.92 eV, indicating the capability of the former for capturing visible light, comparatively. In wolframite-structured tungstates the upper part of the valence band consists mainly of the O$^{2-}$ 2p states, and the conduction band is dominated by the W$^{6+}$ 5d states, in a similar way as it occurs in WO$_3$ [34]. Including the transition metal Ni in tungsten to form tungstate invokes the O$^{2-}$ 2p states and the W$^{6+}$ 5d to hybridize with d electrons of the Ni$^{2+}$ cation. The smaller band-gap of the samples could be caused by the larger contribution of the metal states to the valence and conduction bands [35]. The UV–vis spectra allow for discrimination between mildly distorted isolated WO$_4$/WO$_6$ ($E_g$ > 4.4 eV) and polymeric structures ($E_g$ < 4.0 eV) [29]. Decreasing $E_g$ values than 4 eV in our synthesized materials invokes that they are mainly tungstate compounds (NiWO$_4$). The shift of the absorption edge in NiW$_{1SS}$ to $E_g$ of 2.23 eV
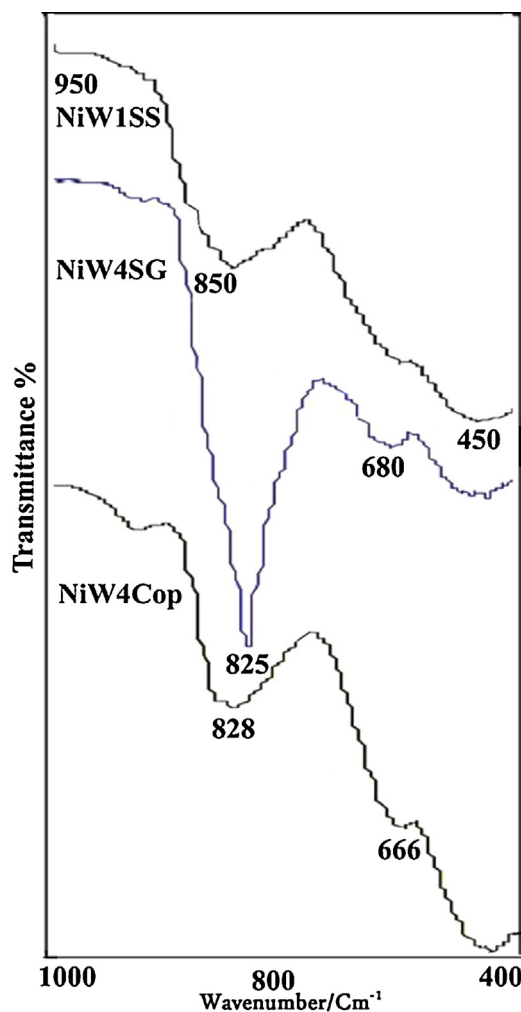


**Fig. 5.** Energy gap ($E_g$) values of NiW$_{1SS}$, NiW$_{4SG}$ and NiW$_{4Cop}$.



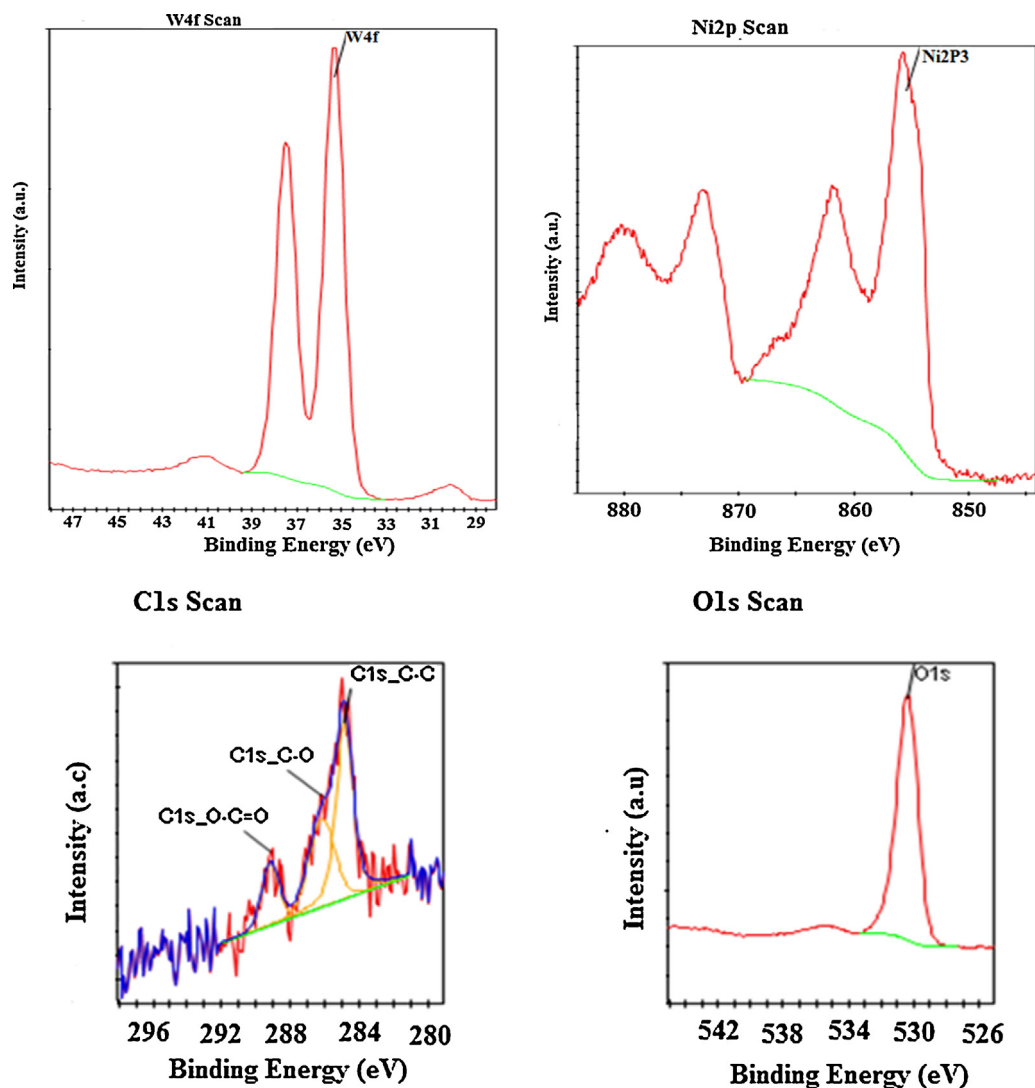**Fig. 6.** FTIR spectra of NiW$_{1SS}$, NiW$_{4SG}$ and NiW$_{4Cop}$.

**Fig. 7.** X-ray photoelectron spectra of W4f, Ni2P, C1s and O1s transitions of the NiW$_{4SG}$ material calcined at 400 °C.

compared to 2.56 and 2.92 eV for NiW$_{4SG}$ and NiW$_{4Cop}$ respectively, is correlated to the increase in particle size of the former comparatively as depicted from XRD and TEM results, reflecting that narrowing the energy gap is due to quantum size effects. The shift of the absorption edge in nano NiW$_{4Cop}$ to higher energies compared to NiW$_{4SG}$ is also devoted to the increase in particles size of the former (Table 1) comparatively. It is well known that, as a consequence of quantum confinement of the photogenerated electron–hole pairs, the UV–vis absorption spectra of semiconductor nanoparticles are size dependent [36]. Particularly, the wavelength at the maximum exciton absorption ($\lambda_{max}$) decreases because of the decrease of the nanoparticles size [37]. This was not affirmed for the NiW$_{4Cop}$ sample that expected to own the lowest optical band gap since it showed the lowest maximum absorption between all samples. This was due to the evolution of some other phases beside NiWO$_4$ such as low crystalline WO$_3$ nanoparticles that causes widening of the energy gap. This points out that WO$_3$ nanoparticles; of decreased particle size, and in close proximity to NiWO$_4$ in NiW$_{4Cop}$ could cause an increase in band gap energy due to quantum confinement effect [38] unlike the case in NiW$_{4SG}$ in which well crystallized WO$_3$ decreased the $E_g$ of NiWO$_4$.

The IR spectra of calcined samples are shown in Fig. 6. In the IR spectrum of the NiW$_{1SS}$ sample, broad bands at 950, 850, 666 and 450 cm$^{-1}$ are depicted to confirm the NiWO$_4$ formation where the

band at 950 cm$^{-1}$ is ascribed to the stretching modes of the W=O terminal bond present in each octahedron of WO$_3$ [39]. Since XRD results of the sample indicated the presence of negligible amounts of low crystalline WO$_3$ hence this band is likely to be the highly dispersed WO$_3$ species. This may also indicate that the material has a high long-range disorder with some short-range order. This was in conformity with the assignment of the 739 nm band depicted for the same sample when using UV–vis spectroscopy technique. The absence of bands at 805 and 750 cm$^{-1}$ due to stretching vibrations of bridging W—O—W bonds [40] confirms the assignment concerning the NiWO$_4$ formation. Additionally, the observed band at 450 cm$^{-1}$ confirms the stretching vibrations of the NiO$_6$ polyhedra building NiO [41,42], validating the formation of NiWO$_4$ structure. In the NiW$_{4Cop}$ sample, the band at 950 cm$^{-1}$ is appeared, in conformity with XRD results, together with broad bands at 828, 450 and 666$_{sh}$ cm$^{-1}$. The vibrational spectrum of the NiW$_{4SG}$ sample presented typical bands as in NiW$_{4Cop}$ at 825, 680 and 450 cm$^{-1}$ except that at 666 cm$^{-1}$ in the later is shifted to 680 cm$^{-1}$ in the former and became broader. The broadness of the 680 cm$^{-1}$ band explains that NiWO$_4$ in NiWO$_{4SG}$ was not completely pure probably due to its association with the crystalline WO$_3$ phase [43,44]. An evidence of the formation of the WO$_3$ phase in the NiWO$_{4SG}$ sample was also depicted by the broad band at 950 cm$^{-1}$, in conformity with XRD and DRS investigations. It is interesting reporting that IR spectra
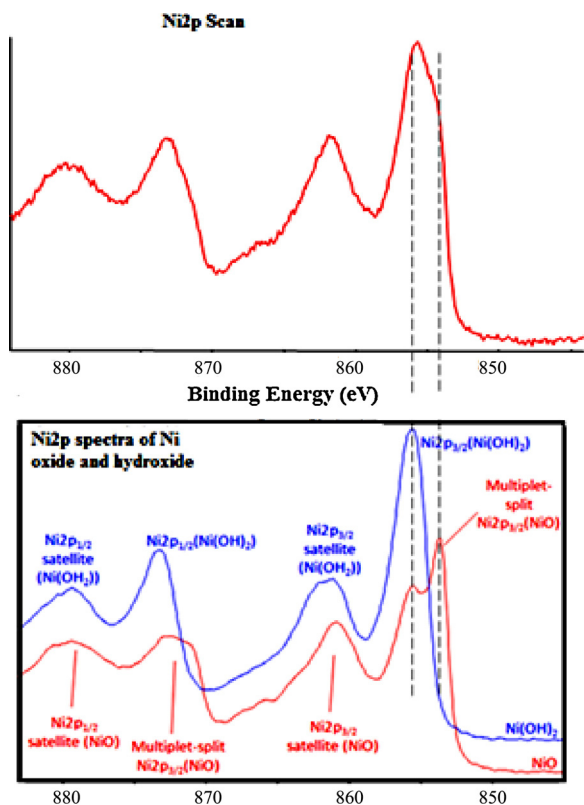
**Fig. 8.** Peak fitted Ni2p signals to NiO and Ni(OH)$_2$ in NiW$_{4SG}$ sample calcined at 400 °C.
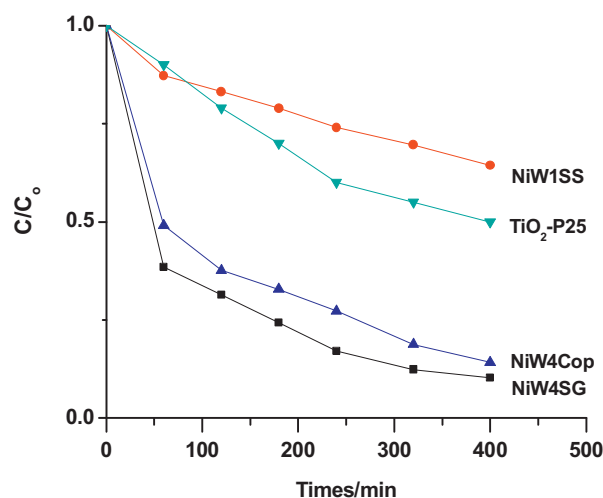


**Fig. 9.** Change in the relative dye concentration vs. time for the synthesized NiWO$_4$ photocatalysts (reaction conditions: 350 ml of 20 ppm MB, 200 mg catalyst, 750 rpm).

of our synthesized samples showed bands in the 1338–1775 cm$^{-1}$ region due to residual organics as a result of the incomplete decomposition of the templates (see supporting information) and this was in conformity with TGA data.

## 3.4. XPS analysis

Fig. 7 shows the spectra of Ni2p3/2 and W4f7/2 of the NiW$_{4SG}$ catalyst annealed at 400 °C. The asymmetric Ni2p3/2 XPS main peak seen at 855.4 eV shows one additional structure at the high BE side, named satellite peak at 862 eV. This is suggestive of multiple oxidation states of Ni. The Ni2p spectrum is compared to two reference spectra from NiO and Ni(OH)$_2$ (Fig. 8). The NiO reference spectrum has a peak at about 854 eV, which is seen in the NiW$_{4SG}$ sample as a shoulder [45]. It has also a sharper satellite line at about 860 eV, resemble that in the same spectrum, along with a shoulder at ~866 eV. The Ni(OH)$_2$ reference spectrum has a broad peak at 855.5 eV, which is close to the maximum of the NiW$_{4SG}$ sample. The broader satellite at 860 eV does not resemble that of NiW$_{4SG}$ in a firm way, so if Ni(OH)$_2$ is present, it is not the dominant component. Based on these reference data, the reasonable interpretation of NiW$_{4SG}$ is most likely being predominantly NiO, with an additional state that could be Ni(OH)$_2$, or something that causes a similar shift in the Ni2p peak. This could account for a different local environment of the Ni atoms in the bulk structure, influencing the Ni—O interaction. The shift of Ni2p to higher BE compared with Ni rich samples [46] is very much related to the presence of tungsten atoms in the structure of the Ni—W—O catalyst nearby the surface of the material, as can be seen in NiW$_{1SS}$ (856.2 eV, Table 2). Exceeding the BE of the latter band in NiW$_{1SS}$ to higher values is probably due to the presence of Ni$^{3+}$ provoking its existence on the synthesis method used [47].

Indeed, IR and XRD results confirmed the presence of NiWO$_4$. In addition, the BE of the Ni2p3/2 XPS secondary peaks clearly change with increasing tungsten content in the sample (Table 2). This could account for a different local environment of the Ni atoms in the bulk structure [48]. Fig. 7 also shows that the W4f spectra in our sample consist of well-resolved spin orbit split doublet peaks corresponding to W4f7/2 at 35.6 eV, and W4f5/2 at 37.5 eV, close to the binding energy for W4f7/2 in NiWO4 [16,18], i.e. resembling that of W$^{6+}$. A shift to lower BE in the W4f7/2 main peak in the sequence NiW$_{1SS}$ > NiW$_{4SG}$ > NiW$_{4Cop}$, compared with that of bulk WO$_3$ [32], with increasing W content, is clearly observed (Table 2). This could be related to the presence of Ni atoms in the local environment of W$^{6+}$ species [23]. XPS data seen in Table 2 confirmed the presence of non-reacted amounts of NiO in NiW$_{4SG}$ and NiW$_{4Cop}$ samples synthesized at a nominal molar ratio of 4 (W/Ni). The ratio between Ni, W, and O in NiW$_{4SG}$ and NiW$_{4Cop}$ samples is not close to the stoichiometric of 4 for W/Ni, unlike that depicted from EDX elemental compositions, proposing the non-homogeneity of the sample.

The C 1s spectrum has been fitted with three components; as shown in Fig. 7, to show chemical states due to hydrocarbon (C—C) and alcohol, ester or carboxylate (C—O, O—C=O). This is not consistent with typical adventitious contamination used to be because of their high amounts, thus it probably came from the non-complete decomposition of the triblock copolymer template as evidenced by the TG technique (not shown). The O 1s peak seen at 530.4 eV indicated the presence of nanosized NiWO$_4$. It is expected that a local structure relaxation in nano-NiWO$_4$ will slightly decrease the O 1s binding energy compared to that of crystalline NiWO$_4$. Moreover the phases with larger O 1s binding energies, such as Ni(OH)$_2$ could contribute to the larger shift towards lower binding energies [49]. This can be related to the appearance of a nickel oxide phase in which oxygen atoms have lower binding energy [50].

## 3.5. Photocatalytic degradation

After equilibration of the dye–photocatalyst suspension in the dark, the photo-degradation of the methylene blue (MB) dye was found to depend on the nature of the synthesized NiWO$_4$ catalysts: 30.0% for NiW$_{1SS}$, 92.5% for NiW$_{4SG}$ and 81% for NiW$_{4Cop}$. The decolourization behaviour of MB on NiWO$_4$ photocatalysts is shown in Fig. 9. It is important to notify that the contact time prior to irradiation was 30 min for all samples and it was 400 min

**Table 2**
XPS results including surface composition (at %) for synthesized $NiW_{1SS}$, $NiW_{4Cop}$ and $NiW_{4SG}$ catalysts.
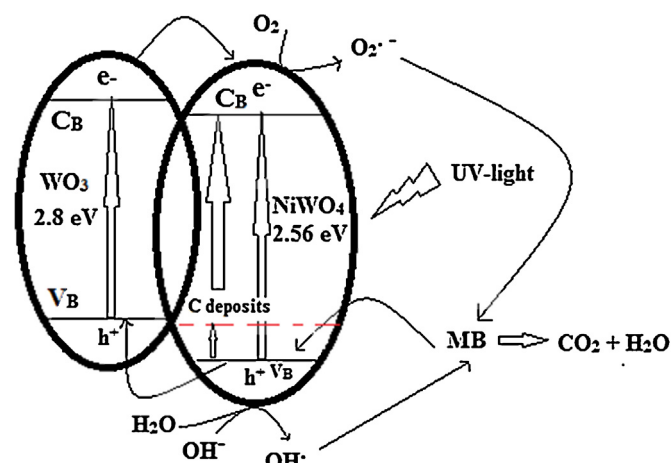
| Sample | Ni2p3/2 main peak (eV) | Ni2p3/2 secondary peak (eV) | W4f7/2 main peak (eV) | W4f7/2 secondary peak (eV) | Ni% from Ni2p | W% from W4f | O% from O1s |
|---|---|---|---|---|---|---|---|
| $NiW_{1SS}$ | 856.2 | 861 | 35.56 | 37.43 | 8 | 9 | 35 |
| $NiW_{4SG}$ | 855.4 | 862.2 | 35.33 | 37.5 | 8 | 19 | 36 |
| $NiW_{4Cop}$ | 855.3 | 863 | 35.21 | 37.35 | 6 | 17 | 41 |

during the MB photo-oxidation reaction. This is very important to reveal the effect of surface area and particle size of the samples while performing the reaction. It is observed that $NiW_{4SG}$ is the most active while $NiW_{1SS}$ is the least active photocatalyst for the degradation of MB even when compared with P25 $TiO_2$ that presented activity composed of 46%. From the plot (not shown) of the decolourization rate vs. the irradiation time, straight lines can be fitted in the first part of the plots, estimating apparent first order kinetic constants of 0.017, 0.012 and 0.003 $min^{-1}$ for $NiW_{4SG}$, $NiWO_{4Cop}$ and $NiW_{1SS}$, respectively. It can be seen that the surface area of the materials has an opposite trend with respect to that revealed by the amount of MB degraded on the photocatalysts since $NiW_{4SG}$ that exhibited the lowest surface area value presented the highest activity. Accordingly, calculated turn over frequency expressed per unit total area of catalysts was $0.18 \times 10^{-3}$, $0.57 \times 10^{-4}$ and $0.17 \times 10^{-4}$ mmol $m^{-2}$ $min^{-1}$ for $NiW_{4SG}$, $NiW_{4Cop}$ and $NiW_{1SS}$, respectively. The low activity of $NiW_{1SS}$ (having band gap of 2.23 eV) towards the degradation of MB may be related to the inaccessibility of the catalysts to the photons of the wavelength needed to generate oxidizing species since MB in solution acts as a shield for absorbing incoming photons, hindering the direct interaction of photons with the photocatalyst. On the contrary, $NiW_{4Cop}$ and $NiW_{4SG}$ those showed higher band gaps encompassing the range from 2.56 to 2.92 eV exhibit lower adsorption comparatively and thus allowed the energy transfer by the excited dye molecules. It is well established [51] that the adsorption in the dark of a substrate on the surface of the semiconductor acts a vital role in its degradation under irradiation. In fact, the amount of the dye adsorbed in the dark provides a rough estimation of the nature and number of available adsorption sites present at the surface of the catalyst. This parameter is not easily evaluated under irradiation since additional adsorption sites may be generated with the possible formation of surface defects [52]. A rather high adsorption of the substrates must be guaranteed in order to efficiently promote their degradation, while the complete surface coverage is often detrimental, as was observed in the case of $NiWO_4$ in the work of Fornasiero et al. [53]. In this case, the dye acts as a shield, hindering the direct photon absorption leading to an inactive catalyst. In the later work [53], the catalytic activity of $NiWO_4$ was not evaluated, since the catalyst surface was fully covered by adsorbed MB reaching great values as high as 92% where it gives activity comprised of 10% degradation in case of methyl orange dye. Accordingly, the differences in the photocatalytic activity in our tungstates can be ascribed to exceeding the adsorption on $NiW_{1SS}$ (19.7%) than on $NiW_{4SG}$ and $NiW_{4Cop}$ (10.9–11.5%). Thus, we believe that the reactivity on the later catalysts is mainly due to electronic properties rather than adsorption ones. Increasing the adsorption on $NiW_{1SS}$ comparatively could be due to the presence of appreciable amounts of the amorphous $WO_3$ in conformity with the work of Luo et al. [54]. This let us presume that sever adsorption will inhibit the production of oxidizing species, through water oxidation, irrespective of lowering the $E_g$ of the $NiW_{1SS}$ catalyst; comparatively, and thus prohibits reaching the photons into the surface. In consistence, the comparison of the performance of the Degussa P25 $TiO_2$ photocatalyst with $NiW_{4SG}$ was significant. This former reference material showed a lower activity 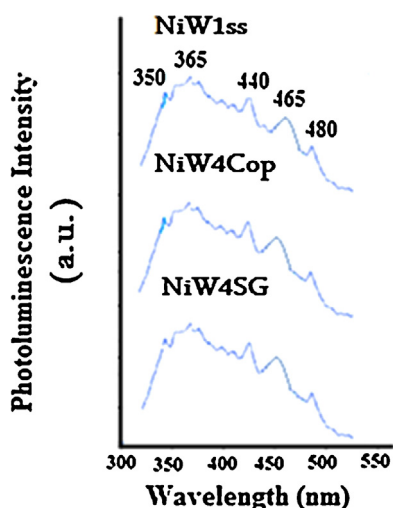($k = 0.0041$ $min^{-1}$) with respect to the latter, probably due to a higher percentage of MB adsorption on its surface (24.8%).

However, as mentioned in the results obtained, the synthesized $NiW_{4SG}$ catalyst exhibits an obvious difference in particle morphology. This decisive difference in morphology that correlated with the decrease in particles size (25 nm) together with the noticed close contact between $WO_3$ and $NiWO_4$ moieties probably influenced the photocatalytic activity, i.e. the exposed crystal faces and/or the ratios among exposed crystal faces (Table 1) are undeniably have decisive influences in inhibiting the recombination between electrons and holes. Accordingly, the finer particles size of $NiW_{4SG}$, the shape as well as the crystalline $WO_3$ species influenced the activity towards MB degradation. The low recombination rate of electrons and holes is also an indispensable reason for exceeding the photocatalytic activity of $NiW_{4Cop}$ than that on $NiW_{1SS}$ since the former shows some crystalline $WO_3$ species [55], which have exceptional chemical and photoelectrochemical stability in aqueous media over a very wide pH range. Accordingly, the enhancement of the photocatalytic activity of $NiW_{4SG}$ and $NiW_{4Cop}$ is due to effective charge separation caused by trapping the photogenerated electrons.

A mechanism for the increase in photocatalysis by $NiW_{4SG}$ is shown schematically in Fig. 10. Under UV illumination, electrons ($e^-$) are excited from the valence band (VB) to the conduction band (CB) of $NiWO_4$, creating a hole ($h^+$) in the VB. Only a small number of electrons and holes usually participate in photocatalytic reactions resulting in a low reactivity, while the rest are lost due to recombination. $WO_3$ mainly absorbs in the near ultraviolet and blue regions of the solar spectrum because of its band gap ($E_g = 2.6$ eV to approximately 2.8 eV) [56]. As a basic function, $WO_3$ has a suitable conduction band potential to allow the transfer of photogenerated electrons to $NiWO_4$ facilitating effective charge separation as well as hindering recombination. It is easy for electrons to transport from $WO_3$ to the $NiWO_4$, because of the close contact and large interface area between them that has been attained via coupling of the $WO_3$ semiconductor with $NiWO_4$.



**Fig. 10.** Scheme for electron–hole separation and transport at UV-light driven $NiWO_4(WO_3)$ photocatalyst interface.

**Fig. 11.** PL spectra (excitation wavelength of 290 nm) for NiWO$_4$ nanoparticles synthesized by different methods.

This is rather surprising results given that previous reports suggest that NiWO$_4$ in its own is either inactive or slightly active in the photocatalytic removal of organics [57,58]. Perceiving such high activity let us presume that residual carbons can act as hole scavenger; as well, to contribute to the apparent activity together with the mentioned parameters discussed above including morphology and the close contact between WO$_3$ and NiWO$_4$ species. In concordance, the TGA diagram of NiW$_{4SG}$ (not shown) evidences the presence of residual organic template following annealing at 400 °C. However, the absence of carbons in XRD results confirms that it is likely to be in an amorphous state. This doping by the non-metallic carbon has shown to result in visible-light sensitization of TiO$_2$ [59,60]. It has been extensively approved that carbon doping would introduce a mid band-gap state close to the TiO$_2$ VB and extends light absorption to longer wavelength region [61]. Therefore, the synthesized carbon-doped NiW$_{4SG}$ hybrid (Fig. 10) with WO$_3$ shows a higher UV light photocatalytic activity towards MB degradation.

In conformity, photoluminescence emissions spectra arise from the recombination of free carriers are carried out for all synthesized catalysts, as shown in Fig. 11. The emissions for all synthesized NiWO$_4$ nano-particles were at wavelength range of 300–500 nm. The observed patterns were similar to other wolframite compounds; Originated from the WO$_6^{6-}$ anion along with some defects in the crystal structure [62]. The emission bands at 350 and 365 nm come from the band gap transition, where the small doublet peaks appear at 400 and 410 are due to either the quantum size [63] and/or to the interference between the luminescence band of the WO$_6$ groups and the absorption band of the NiO$_6$ groups [64]. The obvious emission peaks of 440, 465 and 480 nm are related to the intensive transition from the ground state $^3A_{2g}$ to the excited state $^3T_1$ of Ni$^{2+}$ (3d$^8$) ions [64] in distorted octahedral coordination [65] or due to recombination of e–h pairs localized at oxygen-atom-deficient tungstate ions [66]. The PL emission spectra of the synthesized wolframite NiWO$_4$ nanoparticles show similar peak positions with varied PL intensities. The PL intensity of the NiW$_{1SS}$ sample was significantly higher than those of NiW$_{4Cop}$ and NiW$_{4SG}$. The reason lies in the fact that the PL emission mainly results from the recombination of photo-excited electrons and holes, and then a lower PL intensity might indicate a lower recombination rate of those electrons and holes under light irradiation [67]. Accordingly, the deposition of WO$_3$ on NiWO$_4$ forming hybrid structure in both NiW$_{4cop}$ and NiW$_{4SG}$ nanoparticles reduces PL emission intensity significantly, and thus favours the enhancement

of their photodegradation properties comparatively based on avoiding electron–holes recombination in the WO$_3$/NiWO$_4$ heterojunction.

## 4. Conclusion

It has been shown that the synthesis techniques including simple salt addition, co-precipitation and sol–gel as well as the molar ratio of W/Ni together with the template type including PEG and triblock copolymer affected greatly the characteristics of the produced NiWO$_4$ materials. Of particular interest the existence of WO$_3$ phase, at a molar ratio (W/Ni) of 4, either in amorphous or in well crystalline state beside NiWO$_4$, affects greatly the surface, electronic and morphological properties of the produced catalysts. The NiW$_{1SS}$ material, synthesized at molar ratio of 1 and only exposes NiWO$_4$, indicated monomodal mesoporous distribution as well as the lowest $E_g$ (2.23 eV) between all synthesized tungstates. This elaborates the effect of the PEG template in synthesizing mesoporous structure of nanoplate shape, of average size of 34 nm, and high surface area value. At a nominal molar ratio (W/Ni) of 4, the NiW$_{4Cop}$ and NiW$_{4SG}$ samples those synthesized, respectively using PEG and triblock copolymer templates presented different properties. In particular, the latter material presented macropores and mesopores of nanoflake shape, average sizes of 25 nm, and well crystallized WO$_3$ in close contact with NiWO$_4$, and thus exhibited $E_g$ value of 2.56 eV. The former indicated amorphous WO$_3$ that widen the $E_g$ of NiWO$_4$ to 2.92 eV. Despite its large band gap comparatively, NiW$_{4SG}$ presented the highest photocatalytic activity (92.5%); ever reached for the first time, among all synthesized nickel tungstates studied so far in the degradation of MB. The higher activity of NiW$_{4SG}$ for the degradation of MB was correlated to the increase in the lifetime of the electron–hole pair facilitated by the presence of WO$_3$ crystallites; as confirmed by PL spectroscopy, due to the strong heterojunction with NiWO$_4$ and to decreasing the crystallites size. This study proved that they are a new class of inspired photocatalysts that are worthy to be further studied and can be a valuable addition in photocatalyst collection in future.

## Appendix A. Supplementary data

Supplementary data associated with this article can be found, in the online version, at http://dx.doi.org/10.1016/j.apcatb.2013.12.001.

## References

[1] W. Carel, E. Eijk, Nucl. Instrum. Methods Phys. Rev. A 392 (1997) 285–291.
[2] R. Sundaram, K.S. Nagaraja, Mater. Res. Bull. 39 (2004) 557–565.
[3] H. Wang, F.D. Medina, Y.D. Zhou, Q.N. Zhang, Phys. Rev. B 45 (1992) 10356–10361.
[4] J.M. Quintana-Melgoza, A. Gomez-Cortes, M. Avalos-Borja, React. Kinet. Catal. Lett. 76 (2002) 131–140.
[5] B. Scheffer, P. Molhoek, J.A. Moulijn, Appl. Catal. 46 (1989) 11–19.
[6] M.N. Mancheva, R.S. Iordanova, D.G. Klissurski, G.T. Tyuliev, B.N. Kunev, J. Phys. Chem. C 111 (2007) 1101–1107.
[7] J.M. Quintana-Melgoza, J. Cruz-Reyes, M. Avalos-Borja, Mater. Lett. 47 (2001) 314–321.
[8] A. Kuzmin, J. Purans, Electrochim. Acta 46 (2001) 2233–2239.
[9] G.W. Smith, J. Ibers, Acta Crystallogr. 19 (1965) 269–275.
[10] M. Daturi, G. Busca, M.M. Borel, A. Leclaire, P. Piaggio, J. Phys. Chem. B 101 (1997) 4358–4365.
[11] L. Weber, U. Egli, J. Mater. Sci. 12 (1977) 1981–1988.
[12] K.T. Jacob, J. Mater. Sci. 12 (1977) 1647–1654.
[13] A. Sen, P. Pramanik, J. Eur. Ceram. Soc. 21 (2001) 745–751.
[14] J.H. Pyu, J.W. Yoon, C.S. Lim, W.C. Oh, K.B. Shim, Ceram. Int. 31 (2005) 883–889.
[15] A.L.M. de Oliveira, J.M. Ferreira, M.R.S. Silva, G.S. Braga, L.E.B. Soledade, M.A.M.A. Maurera, Dyes Pigments 77 (2008) 210–216.
[16] A. Sen, P.A. Pramanik, J. Eur. Ceram. Soc. 21 (2001) 745–753.
[17] H. Fu, C. Pan, L. Zhang, Y. Zhu, Mater. Res. Bull. 42 (2007) 696–703.
[18] S.H. Yu, B. Liu, M.S. Mo, J.H. Huang, X.M. Liu, Y.T. Qian, Adv. Funct. Mater. 13 (2003) 639–646.

[19] J. Lin, J. Lin, Y. Zhu, Inorg. Chem. 46 (2007) 8372–8378.
[20] G. Huang, Y. Zhu, Mater. Sci. Eng. B: Solid 139 (2007) 201–209.
[21] G. Huang, C. Zhang, Y. Zhu, J. Alloys Compd. 432 (2007) 269–276.
[22] G. Huang, Y. Zhu, J. Phys. Chem. C 111 (2007) 11952–11958.
[23] B. Solsona, A. Dejoz, M.I. Vázquez, F. Ivars, J.M. López Nieto, Top. Catal. 52 (2009) 751–757.
[24] T. Montini, V. Gombac, A. Hameed, L. Felisari, G. Adami, P. Fornasiero, Chem. Phys. Lett. 498 (2010) 113–119.
[25] B. Solsona, J.M. López Nieto, P. Concepción, A. Dejoz, F. Ivars, M.I. Vázquez, J. Catal. 280 (2011) 28–36.
[26] P. Du, J.A. Moulijn, G.J. Mul, J. Catal. 238 (2006) 342–349.
[27] M.M. Mohamed, S.M.A. Katib, Appl. Catal. A: Gen. 287 (2005) 236–244.
[28] E.I. Ross-Medgaarden, I.E. Wachs, J. Phys. Chem. C 111 (2007) 15089–15096.
[29] J.L.G. Fierro (Ed.), Metal Oxides: Chemistry and Applications, CRC Press/Taylor & Francis Group/LLC, Boca Raton, FL, 2006, pp. 1–30.
[30] M.F. Daniel, B. Desbat, J.C. Lassegues, B. Gerand, M. Figlarz, J. Solid State Chem. 67 (1987) 235–243.
[31] W. Morales, M. Cason, O. Aina, N.R. de Tacconi, K. Rajeshwar, J. Am. Chem. Soc. 130 (2008) 6318–6319.
[32] T. Nanba, S. Takano, I. Yasui, T. Kudo, J. Solid State Chem. 90 (1991) 47–54.
[33] E. Cazzaneli, C. Vinegoni, G. Mariotto, A. Kuzmin, J. Purans, Solid State Ionics 123 (1999) 67–75.
[34] E. Orhan, M. Anicete-Santos, M.A.M.A. Maurera, F.M. Pontes, A.G. Souza, J. Andrès, Solid State Chem. 178 (2005) 1284–1291.
[35] R.L. Frost, L. Duong, M. Weier, Spectrochim. Acta A 60 (2004) 1853–1859.
[36] K. Nakamoto (Ed.), Infrared and Raman Spectra of Inorganic and Coordination Compounds, Wiley, New York, 1980.
[37] P.K. Pandey, N.S. Bhave, R.B. Kharat, Electrochim. Acta 51 (2006) 4659–4666.
[38] M.N. Mancheva, R.S. Iordanova, D.G. Klissurski, G.T. Tyuliev, B.N. Kunev, J. Phys. Chem. C 111 (2007) 1101–1108.
[39] P. Cailet, P. Saumagne, J. Mol. Struct. 4 (1969) 351–358.
[40] N.T. McDevitt, W.L. Baun, Spectrochim. Acta 20 (1964) 799–806.
[41] A. Kuzmin, A. Kalinko1, R.A. Evarestov, Cent. Eur. J. Phys. 9 (2011) 502–509.
[42] V.V. Fomichev, O.I. Kondratov, Spectrochim. Acta A 50 (1994) 1113–1119.
[43] M. Maczka, J. Kanuza, S. Kojima, J.H. Van der Maas, J. Solid State Chem. 158 (2001) 334–341.
[44] E. Heracleous, A.F. Lee, K. Wilson, A.A. Lemonidou, J. Catal. 231 (2005) 159–167.
[45] T.H. Fleisch, G.J. Mains, J. Chem. Phys. 76 (1982) 780–787.
[46] E. Brescacin, M. Basato, E. Tondello, Chem. Mater. 11 (1999) 314–321.
[47] A.F. Carley, S.D. Jackson, J.N. Oshea, M.W. Roberts, Surf. Sci. 440 (1999) L868–L874.
[48] M. Sun, N. Xu, Y.W. Cao, J.N. Yao, E.E. Wang, J. Mater. Res. 15 (2000) 927–935.
[49] E. Salje, A.F. Carley, M.W. Roberts, J. Solid State Chem. 29 (1979) 237–245.
[50] J. Haber, J. Stoch, L. Ungier, J. Solid State Chem. 19 (1976) 113–120.
[51] A.L. Linsebigler, G. Lu, J. Yates, Chem. Rev. 95 (1995) 735–748.
[52] I. Othman, R.M. Mohamed, I.A. Ibrahiem, M.M. Mohamed, Appl. Catal. A 299 (2006) 95–103.
[53] M. Tiziano, G. Valentina, A. Hameed, F. Laura, A. Gianpiero, P. Fornasiero, Chem. Phys. Lett. 498 (2010) 113–119.
[54] J.Y. Luo, Z. Cao, F. Chen, L. Li, Y.R. Lin, B.W. Liang, Q.G. Zeng, M. Zhang, X. He, C. Li, Appl. Surf. Sci. 287 (2013) 270–275.
[55] M. Walter, C. Michael, A. Olawunmi, R.T. Norma, R. Krishnan, J. Am. Chem. Soc. 130 (2008) 6318–6319.
[56] H. Farsi, S.A. Hosseini, J. Solid State Electrochem. 17 (2013) 2079–2086.
[57] U.M. Garcia-Perez, A. Martinez-de la Cruz, J. Peral, Electrochim. Acta 81 (2012) 227–232.
[58] M.M. Mohamed, B.H.M. Asghar, H.A. Muathen, Catal. Commun. 28 (2012) 58–63.
[59] M.M. Mohamed, M.S. Al-Sharif, Appl. Catal. B 142–143 (2013) 432–441.
[60] K. Yang, Y. Dai, B. Huang, M.H. Whangbo, J. Phys. Chem. C 113 (2009) 2624–2629.
[61] V.N. Kolobanov, Nucl. Instrum. Methods A 486 (2002) 496–501.
[62] D.V. Bavykin, S.N. Gordeev, A.V. Moskalenko, A.A. Lapkin, F.C. Walsh, J. Phys. Chem. B 109 (2005) 8565–8570.
[63] A. Kalinko, A. Kotlov, A. Kuzmin, V. Pankratov, I. Anatoli, A.I. Popov, L. Shirmane, Cent. Eur. J. Phys. 9 (2011) 432–437.
[64] A.L.M. De Oliveira, Dyes Pigments 77 (2008) 210–217.
[65] H. Weitzel, H. Z. Kristallogr. 144 (1976) 238–243.
[66] Z. Lou, J. Hao, M. Cocivera, J. Lumin. 99 (2002) 349–453.
[67] R. Sundaram, K.S. Nagaraja, Mater. Res. Bull. 39 (2004) 581–590.